

IE-Map: A novel in-vivo atlas template of the human inner ear

Seyed-Ahmad Ahmadi^{a,b,c,✉}, Theresa Raiser^{a,d,✉}, Ria Maxine Rühl^{a,c}, Virginia L. Flanagin^{a,d}, Peter zu Eulenburg^{a,d}

^a*German Center for Vertigo and Balance Disorders (DSGZ),
Fraunhoferstr. 20, 82152 Planegg, Germany*

^b*Faculty of Informatics, Technical University of Munich,
Boltzmannstr. 3, 85748 Garching, Germany*

^c*Department of Neurology, Klinikum der Universität München,
Marchioninistr. 15, 81377 Munich, Germany*

^d*Graduate School of Systemic Neurosciences, Ludwig-Maximilians-Universität München,
Großhaderner Str. 2, 82152 Planegg, Germany*

Abstract

Brain atlases and templates are core tools in scientific research with increasing importance also in clinical applications. Advances in neuroimaging now allowed us to expand the atlas domain to the vestibular and auditory organ, the inner ear. In this study, we present IE-Map, an in-vivo template and atlas of all known substructures of the human labyrinth derived from multi-modal high-resolution magnetic resonance imaging data in a non-invasive manner (no contrast agent or radiation). We reconstructed a common template from 126 inner ears (63 normal subjects) and annotated it with 94 established landmarks and semi-automatic segmentations. Quantitative substructure analysis revealed a correlation of labyrinth parameters with total intracranial volume. No effects of gender or laterality were found. We provide the validated templates, atlas segmentations, surface meshes and landmark annotations as open-access material, to provide neuroscience researchers and clinicians in neurology, neurosurgery, and otorhinolaryngology with a widely applicable tool for computational neuro-otology.

Keywords: neuro-otology, morphological template, atlas, inner ear,

*Corresponding author: aahmadi@med.lmu.de

**Seyed-Ahmad Ahmadi and Theresa Raiser contributed equally to this work.

membraneous labyrinth, cochlea

1. Introduction

The pervasiveness of brain imaging techniques across many disciplines has increased the relevance of standardized templates of brain structures and developing atlases for the structural and functional substructures within these templates. Almost the entire human central nervous system has been mapped: various templates and atlases have charted out the human cortex, the subcortical nuclei, charting the thalamus and the cerebellum [1, 2, 3, 4] based on MRI. Recently, a dedicated neuroimaging template was also developed for the brain stem and spinal chord [5]. These templates provide a means to make group comparisons and to do quantitative assessments of individual patients, and as such have found applications in neurology [6, 7], in neurosurgery [8, 9] and in neuroscience [10]. In comparison, few works have proposed templates and corresponding atlases to chart the anatomy of sensory organs like the inner ear, and the few existing studies have focused on ex-vivo imaging using (micro-)CT, for comparative neuroanatomy in the field of anthropology.

The inner ear contains several important substructures [11, 12]: (1) The three semicircular canals with their ampullae that shelter the cupula containing the sensory hair cells, which detect head rotation. (2) The macular organs (utricle and saccule), which respond to translational head motion and convey the gravitational force vector [13]. Anatomically, the utricle and the saccule together form the vestibule. (3) The cochlea, which is a separate inner ear organ for hearing. The cochlea consists of the scala vestibuli, the scala tympani and the cochlear duct (with hair cells). These structures spiral 2.57 ± 0.28 times from the base to the cochlear cupula, or apex of the cochlea [12]. Physiological and morphological alterations of the cochlea can result in hearing deficits or loss whereas affections of the semicircular canals or otoliths lead to vertigo and balance disorders [14, 15]. The shape of the labyrinth structures carries valuable functional and phylogenetic information about the inner ear over the course of

mammalian evolution [16]. Inner ear imaging aids neurological examination and neuroscientific analysis. A quantitative assessment of the inner ear organs often requires a preceding segmentation of the relevant target regions and a sub-parcellation into its key structures like the semicircular canals, vestibule and cochlea. As has been shown for brain images, segmentation with a template image and atlas is a versatile and robust tool for anatomic delineation [17]. Beyond deformable atlas segmentation, image templates and structural atlases are fundamental tools for statistical shape analysis [18, 8] and group-based image analysis [19].

Previous anatomical and morphological analyses of the inner have emphasised the cochlea and avoided the complex anatomy of the peripheral vestibular system. Models of the cochlea have been assessed for cross-species comparative neuroanatomy [16, 20, 21, 22], neuronavigation of cochlear electrode implantation and simulation [23, 24, 25], cochlear shape modeling and surgical trauma assessment [12]. In the field of anthropology, previous studies have investigated the inner ear through shape comparison of labyrinthine structures in ancient Egyptian mummies versus today [26], or in form and function of the mammalian inner ear across species [27].

The majority of these analyses were based on ex-vivo micro-CT as the imaging modality [28, 29], few also providing cyto-architecture scans based on synchrotron radiation [30] or ex-vivo ultra-high-field MRI [31]. A few studies have reported detailed measurements of the inner ear's membranous structures [32], and of the semicircular canals in particular, again based on ex-vivo micro-CT [33, 21] and multi-detector CT [34]. Recently, in-vivo visualization of the inner ear with MRI, either with [35, 36] or without Gadolinium-based contrast agents [37, 38, 39, 40, 41] has been used for the detection of endolymphatic hydrops [39] and for diagnosis of sensorineural hearing loss associated with inner ear lesions [42]. Furthermore, MRI sequences, such as *Constructive Interference in Steady State* (CISS) imaging, which have low susceptibility and a high contrast-to-noise ratio, have been used to image the inner ear for the detection of leakage of labyrinthine and cerebrospinal fluids [43].

The purpose of this study was to build a template and atlas of the human inner ear and its substructures, based on multiple non-invasive in-vivo MRI sequences. By harnessing the signal and contrast-to-noise advantages of multiple MRI sequences, all without invasive contrast agents or radiation, we believe the inner ear imaging procedures and corresponding template will have a widespread clinical applicability. We then demarcated the anatomical substructures of the inner ear by registering a previously available inner ear atlas, based on micro-CT, to our template. With this atlas, quantitative size and volume information of the inner ear substructures can be extracted for each individual and side. After validation of the template and atlas with the previous literature, we demonstrate the usability of the template and atlas by examining three questions about the population statistics of the inner ear. 1. Does head size, as measured by intracranial volume, influence labyrinth measurements? 2. Does gender have an effect in inner ear structure size? 3. Does ear laterality play a role in inner ear dimensions? In summary, we successfully created an inner ear template and atlas that can be applied to a wide range of MRI sequences. Our template and atlas are comprehensive, applicable, accessible, and generalizable, forming the basis for future non-invasive neuroimaging studies of the inner ear under the umbrella term computational neuro-otology.

2. Materials and Methods

2.1. Subject cohort

The template was created from a cohort of 63 healthy, right-handed subjects (32 female, 31 male, age: 26 ± 2.3 years). To make the template and atlas representative and generally applicable to both left and right inner ears, left and right inner ears are treated independently, resulting in 126 inner ears in total that were used for template building. All subjects gave written informed consent regarding participation in this study. The local ethics committee of the Ludwig-Maximilians-Universität, Munich, approved the study in accordance with the latest revision of the Helsinki declaration from 2013.

2.2. *MR imaging and pre-processing*

We acquired multi-modal, isotropic 3D MRI data (whole-head T1- and T2-weighted at 0.75 mm, CISS measurement of the labyrinth at 0.5 mm isotropic) in a clinical 3T scanner with a 64-channel head/neck coil (Siemens Skyra, Erlangen, Germany). The high-resolution T1-weighted MPRAGE sequence was collected with GRAPPA in an interleaved mode and an acceleration factor 2 (TR 2060ms, TI 1040 ms, TE 2.17 ms, flip angle 12 deg., FoV 240 mm, slice thickness 0.75 mm, 256 slices, A-P phase encoding, echo spacing 7.9 ms, bandwidth 230Hz/Px, prescan normalized). A T2-SPACE sequence with varying flip angles (TR 3200 ms, TE 560 ms, FoV 240 mm, slice thickness 0.75 mm, 256 slices, A-P phase encoding direction, GRAPPA acceleration factor 2, echo spacing 4.06 ms, bandwidth 625Hz/Px, prescan normalized) was collected for an optimized contrast between tissue types for the atlas generation, to detect brain pathologies and achieve whole-head coregistration for all data. In addition, we acquired an optimised CISS sequence for labyrinthography (TR = 8.56 ms, TE = 3.91 ms, flip angle = 50 deg., FoV = 150 mm, slice thickness= 0.50 mm, right-left phase encoding direction, sequential multi-slice mode, tune up shimming, activation of head coil elements 5-7 and the cranial neck coil elements only, bandwidth 460Hz/pixel, the average of two repetitions was built, total time of acquisition 13:40 minutes) for achieving the best possible contrast and resolution for inner ear structures.

Head motion was controlled by a dedicated head fixation device (®Pearltec Crania Adult, Schlieren, Switzerland). All MRI image data underwent stringent quality assessment before inclusion in the study, using a state-of-the-art MRI quality control toolkit (MRIQC) [44]. As pre-processing, we performed a correction for MRI field inhomogeneity using the N4 bias correction algorithm [45]. Further, we performed a rigid intra-subject registration of T1 and CISS volumes to the T2 volume, before proceeding to template building. Intra-subject registration was performed using Advanced Normalization Tools (ANTs), with normalized mutual information for multi-modal alignment [19].

Total intracranial volume (TIV) as a potential covariate for head size was

obtained via segmentation of the T1-weighted image with the CAT12 toolbox (version 12.6 release 1450, <http://www.neuro.uni-jena.de/cat/>) of the Structural Brain Mapping group (Christian Gaser, Jena University Hospital, Jena, Germany), a toolbox implemented in SPM12 (v7487, Statistical Parametric Mapping, Institute of Neurology, London, UK).

2.3. Template building

Template building was performed in three steps: 1) full-brain template building and annotation, 2) axial re-orientation of all subjects to the Reid's axial plane, and 3) final inner ear template building. The template building method utilized in steps 1 and 3 is a state-of-the-art algorithm provided by the ANTs toolkit [19]. It is designed for computation of a geodesic mean template that optimally represents the average anatomic shape from a set of input volumes. Critically, all ANTs components are capable of multi-variate image registration, allowing us to fully leverage the multi-sequence appearance of the inner ear and its surrounding anatomy in T1, T2 and CISS MRI during template reconstruction. The high accuracy and robustness of ANTs registration and template normalization methods have been validated by demonstrating state-of-the-art performance in several internationally recognized medical image processing challenges [17, 46].

In the first step, we computed a full-brain template for our cohort using T1- and T2-weighted MRI sequences. For the full-brain template, CISS volumes had to be omitted since they were acquired only within a narrow axial field-of-view (FOV) centred around the inner ear region. In the full-brain template, we manually annotated four landmarks for identification of the Reid's axial plane, i.e. the locations of the infraorbital point and external auditory meatus in the left and right hemisphere [47]. We further placed two landmarks at the locations of the left and right inner ear, for a consistent localization of the inner ears across all subjects. This procedure is illustrated in Fig. 1.

In the second step, we re-oriented source volumes to Reid's standard plane. This was a necessary pre-processing step for the inner ear template building

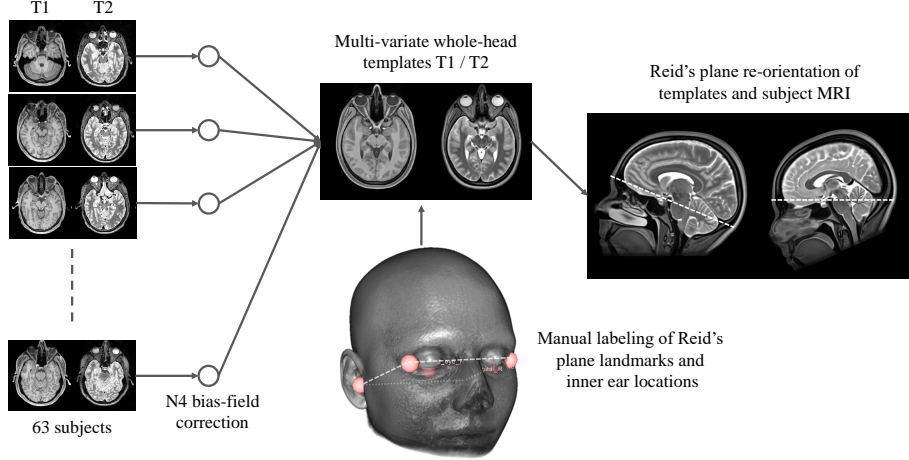


Figure 1: Full-brain template building and annotation, for re-orientation of the axial plane to Reid’s standard plane, and for localization of left/right inner ear region-of-interests (ROI). *(Print in colour.)*

(step 3), which took crops around the inner ear’s region-of-interest (ROI) as input. Pre-aligning these crops resulted in less out-of-border interpolation, i.e. less black margins and a better registration result at the ROI borders during template building. A side benefit of this step was that the lateral semicircular canal became approximately aligned with the axial plane, given the common assumption of coplanarity of the lateral semicircular canals with Reid’s standard plane [48, 49, 50]. The landmarks for Reid’s plane and inner ear FOV centres were transformed into the volumes of all input subjects beforehand, using a full-brain registration from template to individual spaces, followed by visual inspection for quality control. We then computed Reid’s plane parameters using least-squares fitting to the four landmarks, and re-oriented the axial plane in all volumes accordingly.

In the third step, we used the inner ear landmarks identified in step 2 to place region-of-interest (ROI) bounding boxes at the left and right inner ear. At these locations, the T2, CISS and T1 volumes were cropped ($4 \times 4 \times 3$ cm) and resampled (0.2 mm isotropic, bi-cubic B-spline interpolation) with a ROI bounding

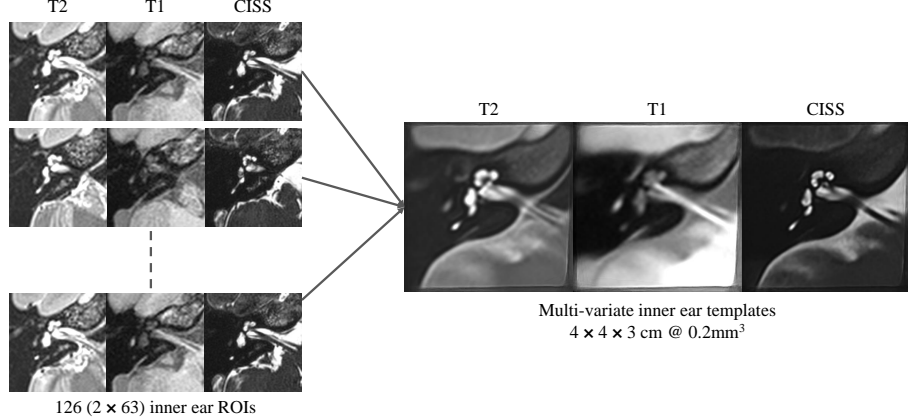


Figure 2: Inner ear template building input: three of 126 example multi-variate inputs (T2, T1, CISS) of the inner ear region are shown, centred, Reid’s plane aligned and cropped with a $4 \times 4 \times 3$ cm ROI. The geodesic mean template is reconstructed and shown on the right side.

box that included all relevant inner ear structures as well as the vestibulo-cochlear nerve. As performed during pre-processing on the full brain volumes, we linearly registered the CISS and T1 crops to the T2 crop, to ensure a perfect alignment of fine structures of the inner ear across all MRI contrasts. Cropped volumes were centred and all left inner ears were mirrored with respect to the sagittal plane, to match the orientation of the right inner ear. This latter step ensured that the obtained template is unbiased with respect to afference laterality (sidedness) of the inner ear structures. The above steps resulted in 126 localized, multi-variate MRI volumes, oriented to Reid’s plane and hence roughly oriented with the lateral semicircular canal in the axial plane. These volumes served as input to the multi-variate template building algorithm, which computed three inner ear templates at an isotropic target resolution of 0.2 mm. The procedure and resulting template are illustrated in Fig. 2.

2.4. *Atlas annotation*

The multi-sequence template was segmented into anatomic regions in order to obtain an atlas of the inner ear. Segmentations were obtained in parts by transferring fine-grained surface meshes of the semicircular canals, vestibule

and cochlea from *Ariadne*, a publicly available atlas and segmentation toolkit of the inner ear derived from ex-vivo micro-CT data [20]. From this toolbox, we leveraged micro-meter accurate surface meshes as delineations of inner ear structures, by registering them to our multi-variate MRI template.

Due to the lack of an accompanying micro-CT intensity volume in the *Ariadne* toolkit, we performed a volumetric registration and geometric transfer through alignment of the entire inner ear's outer surface. For our T2 template volume, we computed the outer iso-surface of the inner ear at an optimal intensity threshold obtained by Otsu's method [51], followed by manual removal of background structures that were obtained during thresholding. For the micro-CT data, we utilized the bony surface mesh provided in the *Ariadne* toolbox. Next, we voxelized both the T2 surface mesh and the micro-CT surface mesh of the inner ear at an isotropic resolution of 0.1 mm, and computed signed Euclidean distance transforms (SDT) for both meshes [52]. These SDT representations served as surrogate image volumes during deformable image registration, yielding a non-linear deformation field from *Ariadne* atlas space into our template space. All micro-CT surfaces including semicircular canals, vestibule, and cochlear ducts (i.e. scala vestibuli, scala tympani and cochlear duct) were then transferred onto our template volume and voxelized at the resolution of 0.2 mm. The resulting labelmap was manually post-processed, based on visual inspection, to ensure alignment of labels with the three intensity channels T2, T1 and CISS.

The cochlea regions were pre-segmented by intensity-based thresholding of the CISS template. The threshold was set to obtain a clear separation of the scala tympani and vestibuli. Both regions were refined manually using basic image processing operations such as connected components, and surface smoothing. The cochlear duct was transformed from the David micro-CT atlas [20] using the computed deformation fields.

The procedures described above were realized using various tools in the open-source software toolkits ANTs (deformable surface registration) [19], 3D Slicer (segment editor effects: threshold, connected components, paint, scis-

sors, margin) [53] and SimpleITK (Euclidean SDT computation with Signed-DanielssonDistanceMapImageFilter) [54].

Using landmark annotation in 3D Slicer [53], we further annotated multiple anatomic landmarks of the inner ear structures described in related literature. For the sake of reproducibility and annotation consistency, we placed all landmarks on the Otsu-threshold iso-surface of the T2 template volume. The landmark locations on the T2 iso-surface are visualized in detail in Fig. 3. Following guidelines and 3D visualizations in [33], we annotated the three semicircular canals regarding width and height, as well as inner widths and heights measured at three positions (Figure 3, panels A and B). We also followed instructions in [33] to compute the height and three width measures of the common crus. The height and width of the vestibule were described in [55]. The total inner ear length was described in [56] (Figure 3, panel C). The placement of landmarks for measurement of cochlea width, length and height was described in [57] (Figure 3, panel D). While cochlear height here was defined on an oblique 3D cut through the volume, earlier approaches defined cochlear height on the coronal plane [58, 59], which we also measured for comparison.

2.5. Statistical methods

First-order group statistics on inner ear dimensions and volumes were computed in terms of mean and standard deviation. Normality of variables throughout this work was tested using a Kolmogorov-Smirnov (KS) test with Lilliefors correction, at an alpha level of $p < 0.05$ [60]. Comparisons of the semicircular canal dimensions between the left and right inner ear sides were performed using multiple paired statistical tests (t-test for normal distributed data, Mann-Whitney U test for non-normal distributions). We corrected p-values after multiple testing using the Benjamini-Hochberg False Discovery Rate (FDR) algorithm [61], results were considered as significant at a post-correction alpha level of $p < 0.05$. For the main general inner ear measures (total inner ear volume, total inner ear length, oblique cochlea height, and radii of anterior/posterior/lateral SCCs), we investigate a potential correlation with overall head size,

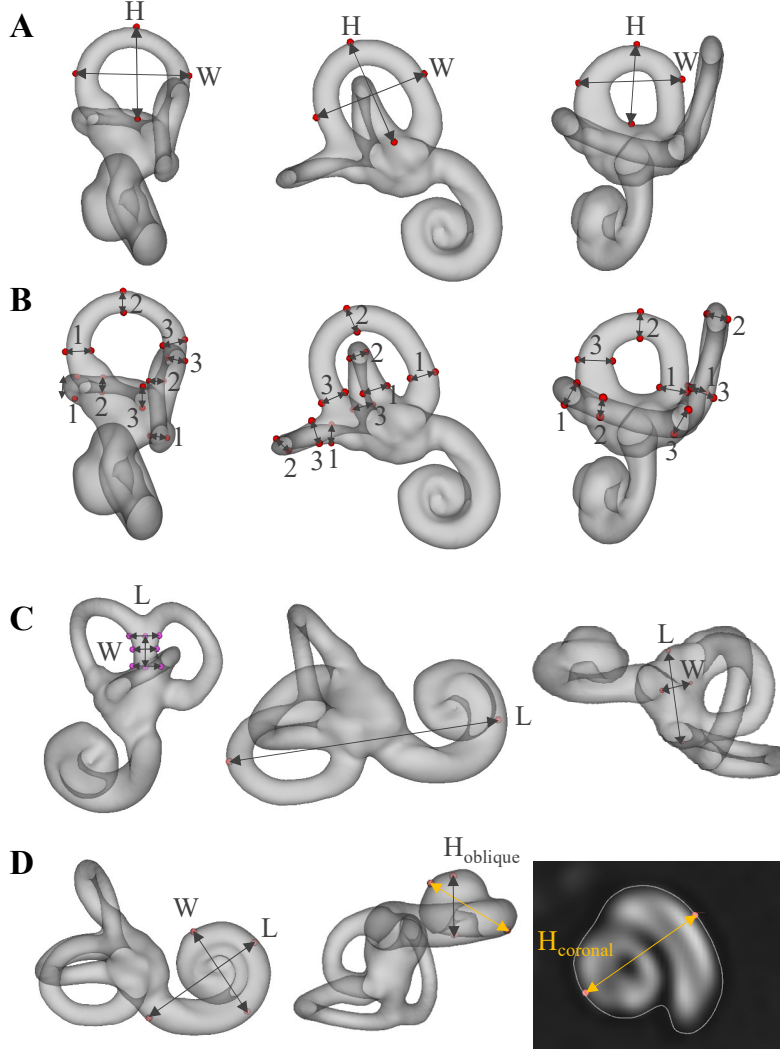


Figure 3: Inner ear landmark annotations in template space. Panel A: width and height of the anterior (left), posterior (middle) and lateral (right) semicircular canals. Panel B: inner widths and heights of semicircular canals, measured at three locations each (1-3). Panel C: height and three widths of the common crus (left), total inner ear length (middle), and vestibule length and width (right). Panel D: width, length and height of the cochlea. Cochlea height was tagged and measured using both the coronal plane approach (gold arrow) [58, 59], and the oblique plane (i.e. 3D) approach (grey arrow) [57]. H = height, W = width, L = length. (Print in colour.)

represented by TIV. Correlation is reported as Pearson's correlation coefficient r , again at a significance level of $p < 0.05$. After clarification of the role of TIV, we tested gender effects, i.e. whether there was a significant difference between male and female cohort subgroups. These tests were performed on the two major inner ear measures, total inner ear volume, total inner ear length. To account for head size, we performed an Analysis of Covariance (ANCOVA), with TIV as the relevant covariate [62]. Statistical computation was performed using python implementations in `scipy.stats` [63], `Pingouin` [64] and `Statsmodels` [65], as well as MATLAB (The Mathworks Inc., MA, USA). Where available and applicable, we provide comparable values from literature that we are aware of, by referencing reported mean and standard deviation values.

3. Experiments and Results

3.1. Inner ear template and atlas

The reconstruction of the T2- and T1-weighted MRI volumes into unbiased full-brain templates was successful. Using this template, the localization of both inner ears and the re-orientation of the axial slice to Reid's standard plane could be executed for all subjects and inner ears without manual intervention. Subsequently, the reconstruction of the T2-, T1-weighted and CISS inner ear template volumes at 0.2 mm isotropic resolution was performed successfully using the ANTs toolkit.

Volume renderings can be seen in Fig. 4. The rendering transfer function was set as a linear ramp between the minimum and maximum voxel intensity for each template, no manual adjustments other than a shift of the centre intensity (T1: 1.2; T2: 1.5; CISS: 2.3) was necessary to achieve the visibility of inner ear structures as displayed. As noticeable from the rendering, the inner structures of semicircular canals, vestibule and cochlea are clearly visible and are morphologically correct. The volume rendering does not suffer from noise artefacts typical in single-subject volumes, which we attribute to the fact that the multi-variate templates on average have a 1.7 times higher signal-to-noise

MRI sequence	Template volumes	Individuals Mean	Individuals SD
T2	4.02	2.49	0.20
CISS	3.26	1.73	0.14
T1	3.13	1.85	0.28

Table 1: Signal-to-noise ratios in multi-variate MRI templates are on average 1.7 times higher than in individuals' volumes, resulting in improved visibility of structural details. Rendering can be performed nearly free of noise (cf. Figure 4), and fine-grained structures like the separation of cochlear ducts become visible in templates that are sometimes not even clearly discernible in individual volumes (cf. Figure 4, panel E).

ratio (SNR) than the mean-SNR in single-subject volumes (see Table 1). SNR is approximated as the mean voxel intensity divided by the standard deviation of voxel intensities inside the inner ear ROI [66].

3.2. Cohort measurements and atlas validation

The characterization of the three semicircular canals (see Table 2) was compared to previously reported results using micro-CT in ex-vivo specimen [33]. In general, our atlas produces larger values than reported in literature, however, the error margin never exceeds the original image resolution of T1- and T2-weighted MRI (0.75 mm). Overall, the sub-voxel accurate distance measures demonstrate that the computed template has morphometric properties that are in line with previously ex-vivo micro-CT studies. The same applies to landmarks of the common crus (see Table 3) and the cochlea (see Table 4), which all corresponded to values in literature within a margin of less than 0.5 mm.

Inner ear volume measurements are also largely in line with related literature (see Table 5), with a notable difference of almost +50 mm³ in total inner ear volume. Deviations from mean volumes reported in [67] can be attributed due to simplified geometric approximations made in that previous study. For example, authors in [67] modelled the ampullae as spheres with 2 mm diameter (i.e. 4.2 mm³; ours: 3.54/2.27/3.59 mm³ for ant/post/lat ampulla), saccule as

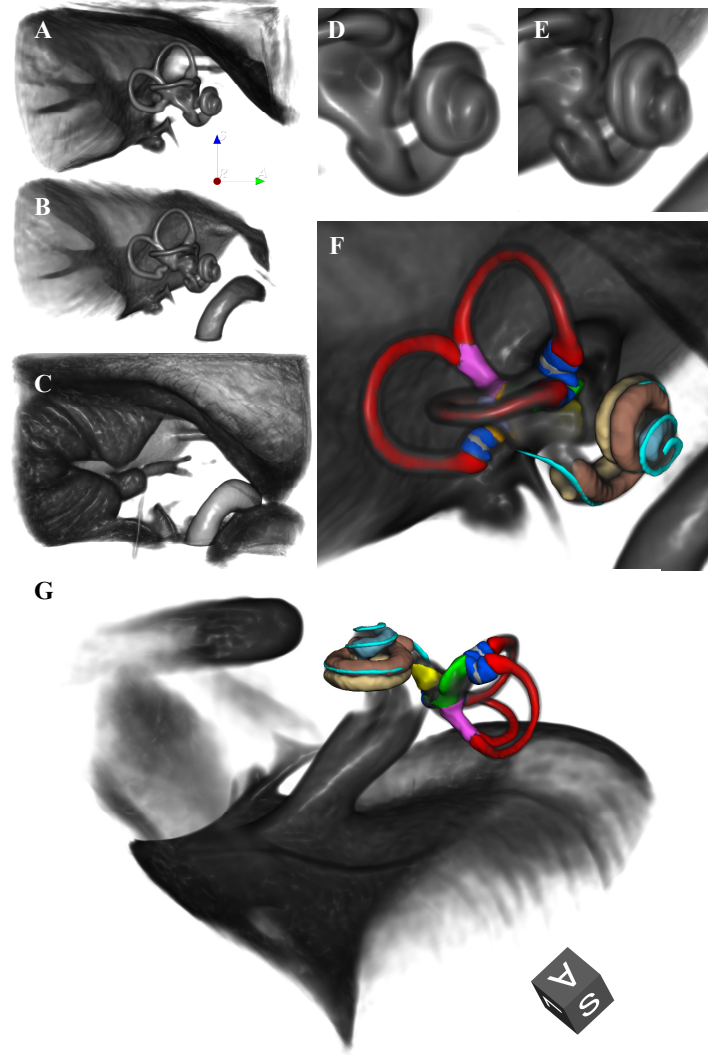


Figure 4: Volume renderings of inner ear templates and atlas (ROI size: $4 \times 4 \times 3$ cm; resolution: 0.2 mm isotropic; viewpoint: right-lateral view onto right inner ear). Panels: A. T2 template; B. CISS template; C. T1 template; D. Closeup cochlea in T2 template; E. Closeup cochlea in CISS template, with a clear separation of scala tympani and vestibuli; F. Atlas surface meshes on CISS template volume rendering. G. Same as F, with a different perspective focussing on the vestibule. Colours and regions: red: semicircular canals; blue: ampullae; pink: common crus; grey: cupula walls; green: utricle; yellow: saccule; brown: scala vestibuli; beige: scala tympani; light blue: cochlear cupula; cyan: cochlear duct. (Print in colour.)

a hemisphere of 2 mm diameter (i.e. 2.1 mm³; ours: 2.6 mm³), utricle as an irregular oval averaging 1.35 mm in diameter and 5.5 mm in length (i.e. 7.9 mm³; ours: 8.8 mm³), and the cochlea as a cone with 8 mm diameter and 5 mm height (i.e. 83.8 mm³; ours: 94.4 mm³). Especially the larger volume measurements of the cochlea and the total inner ear region indicate an increased estimate of the inner ear region by our T2 iso-surface, by 11% and 12%, respectively.

3.3. Cohort analysis and statistics

As detailed in Table 2, paired univariate testing with multiple testing correction yielded no significant differences regarding sidedness in any of the semicircular canals measures (height, width, radius, as well as internal height and width measured at three distinct points from the distal to the common crus). We further investigated the major inner ear dimensions, i.e. total inner ear length, total inner ear volume, oblique cochlea height, and radii of the three semicircular canals. First, we found all these values to be normally distributed (KS-test with Lilliefors correction, $p > 0.05$). Second, we investigated a possible correlation of selected inner ear measures with brain size measured by TIV. We found the total inner ear volume and length, as well as the radii of the anterior and posterior semicircular canals (SCC) to be moderately and significantly correlated with brain size, while the oblique cochlea height and the radius of the lateral SCC were not significantly correlated (cf. Figure 5). Third, we investigated a potential difference between male and female subjects in our cohort regarding the main and most robust inner ear measures, i.e. the total inner ear length and total inner ear volume. Since TIV was found to be a confounding variable for these measures, we performed an ANCOVA, correcting for TIV as a covariate. Our ANCOVA tests yielded no significant differences for the investigated inner ear measures (total inner ear length: $p = 0.182$; total inner ear volume: $p = 0.088$). In other words, after accounting for overall brain size, gender difference cannot explain residual differences in measured inner ear characteristics.

SCC	Dimension	Mean	SD	Mean [33]	SD [33]	Δ Mean	p-val L vs. R
Ant	Height	6.4	0.5	6.5	0.5	0.1	0.074
	Width	8.2	0.5	8.0	0.5	0.2	0.943
	Radius	3.7	0.2	3.6	0.2	0.1	0.088
	Internal width 1	1.8	0.1	1.2	0.2	0.6	0.995
	Internal width 2	1.4	0.2	0.9	0.2	0.5	0.779
	Internal width 3	1.6	0.2	1.2	0.1	0.4	*0.995
	Internal height 1	1.5	0.2	1.0	0.1	0.5	*0.571
	Internal height 2	1.3	0.2	0.7	0.1	0.6	0.943
	Internal height 3	1.6	0.2	0.9	0.1	0.7	0.327
Post	Height	7.0	0.6	6.7	0.6	0.3	0.921
	Width	7.7	0.6	7.7	0.5	0.0	0.695
	Radius	3.7	0.3	3.6	0.2	0.1	0.623
	Internal width 1	1.8	0.1	1.4	0.2	0.4	0.695
	Internal width 2	1.7	0.2	1.5	0.2	0.2	0.995
	Internal width 3	1.6	0.2	1.4	0.2	0.2	*0.995
	Internal height 1	1.4	0.1	1.0	0.1	0.4	0.779
	Internal height 2	1.3	0.2	1.0	0.1	0.3	*0.995
	Internal height 3	1.4	0.2	0.9	0.1	0.5	*0.995
Lat	Height	5.0	0.4	4.9	0.6	0.1	0.088
	Width	6.6	0.4	6.5	0.7	0.1	0.571
	Radius	2.9	0.2	2.9	0.3	0.0	0.088
	Internal width 1	1.8	0.2	2.1	0.3	0.3	*0.716
	Internal width 2	1.7	0.2	1.7	0.3	0.0	*0.995
	Internal width 3	2.2	0.1	1.7	0.2	0.5	0.164
	Internal height 1	1.8	0.2	1.2	0.2	0.6	0.995
	Internal height 2	1.4	0.1	0.8	0.1	0.6	*0.954
	Internal height 3	1.7	0.1	1.2	0.3	0.5	*0.530

Table 2: Dimensions of the anterior (Ant), posterior (Post) and lateral (Lat) semicircular canals (SCC). Unit: [mm]. * indicates non-normal distribution (Kolmogorov-Smirnov test with Lilliefors correction, $p < 0.05$).

RESULTS

ANATOMICAL DIMENSIONS OF THE COMMON CRUS

	Mean	SD	Mean [33]	SD [33]	Δ Mean
Length	2.3	0.2	2.0	0.5	0.3
Width 1	2.2	0.2	1.6	0.3	0.6
Width 2	1.9	0.2	1.5	0.3	0.4
Width 3	2.3	0.2	1.9	0.4	0.4

Table 3: Dimensions of the common crus. Unit: [mm].

Distance	Mean (our)	SD (our)	Mean (lit.)	SD (lit.)	Δ Mean	Reference
Cochlea height coronal	5.58	0.26	5.31	0.52	0.27	[58]
	5.58	0.26	5.11	0.30	0.47	[59]
Cochlea height oblique	3.56	0.22	3.59	0.12	0.03	[57]
Cochlea length	8.92	0.34	9.32	0.53	0.40	[68]
	8.92	0.34	8.84	0.29	0.08	[57]
Cochlea width	6.78	0.31	6.30	0.38	0.48	[57]
Vestibule length	5.39	0.26	5.45	0.54	0.06	[55]
Vestibule width	3.08	0.17	3.20	0.39	0.12	[55]
Inner ear length total	17.59	0.76	17.13	0.64	0.45	[56]

Table 4: Cochlear and other inner ear measurements. Unit: [mm].

Region	Mean	SD	Mean (lit.)	SD (lit.)	Δ Mean	Reference
Ampulla (ant)	3.54	0.43	4.20	n.r.	0.66	[67]
Ampulla (post)	2.27	0.27	4.20	n.r.	1.93	[67]
Ampulla (lat)	3.49	0.45	4.20	n.r.	0.71	[67]
Saccule	2.58	0.41	2.10 / 2.10	n.r.	0.48	[67, 69]
Utricle	8.78	1.12	7.90 / 8.20	n.r.	0.88 / 0.58	[67, 69]
Cochlea	94.42	9.41	83.80	n.r.	10.62	[67]
Inner ear total	269.34	24.67	221.47	24.29	47.87	[56]

Table 5: Inner ear volumes. Unit: $[\text{mm}^3]$. (n.r. = not reported)

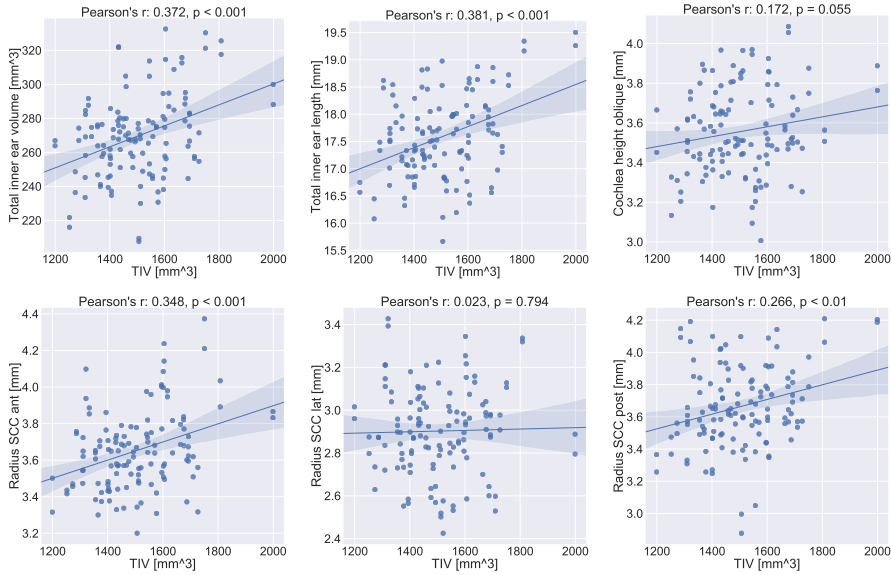


Figure 5: Correlation plots for inner ear measurements with total intracranial volume (TIV). Linear correlation values (Pearson's r) and corresponding p-values are indicated in the subplot titles. The 95% confidence interval for the regression estimate is drawn as a translucent band around the regression line. Total inner ear volume and length, as well as the radii of the anterior and posterior semicircular canals (SCC) are linearly correlated with head size. The oblique cochlea height might well be while the radius of the lateral SCC appears to not be correlated at all with TIV. The results indicate the importance of TIV for future quantitative assessments between cohorts.

4. Discussion

In this work, we presented a human inner ear atlas derived from multi-sequence magnetic resonance imaging in-vivo and non-invasively. To the best of our knowledge, this is the first time a multi-sequence MRI template-atlas-combination of the human labyrinth covering vestibular and auditory structures has been proposed, and the first time its has been constructed from a sizable cohort (>50 subjects). The segmentation and annotation of templates in our work benefitted predominantly from the SNR of the source whole-head T2 images in combination with the high spatial resolution of the CISS sequence. The data analyses resulted in an inner ear atlas uniquely depicting the vestibule (including utricle and saccule), the three semicircular canals and their ampullae, and the cochlea with its three ducts (scala vestibuli, scala tympani and cochlear duct) as well as the cochlear cupula. The TIV was found to be a relevant covariate for measurements of the labyrinth and its substructures. After controlling for TIV as a covariate, no gender or laterality effects were found.

Analogous to the volumetric measures, our reported landmark distances were very much in line with the published literature. We were able to reproduce these landmarks and the distances in-between mainly with the help of detailed illustrations of landmark locations with high-quality 3D visualizations in several works [33, 57], which we followed closely in our work, and which are presented in a similar fashion for comparison purposes in Fig. 3. Earlier descriptions of landmark placement were often based on 2D volume planes, which can be more difficult to understand and reproduce. For example, the cochlear height was previously defined either in the coronal image plane [59, 58], or using an oblique volume cut through the centre of the cochlear basal turn and the cochlear apex [57]. While the former depends on the orientation of the inner ear anatomy with respect to the coronal plane, the latter is uniquely defined in 3D space. Consequently, our measurements of the former has a larger Δ Mean from measurements reported in either [59] or [58], while the measurement of the latter is almost identical to the ones in [57]. A further improvement without going to

higher MRI field strengths is difficult to achieve without a significantly higher voxel resolution in the source material. In any case, an exact replication of reported values in literature is not relevant at this point because i) we relied on a young healthy cohort, while several other works we compared to included pathologies [59, 58, 70] ii) we relied on a single-rater placement of landmarks, and neither we nor related works considered intra- or inter-rater variability on these localizations, and iii) it is not clear yet whether and to what degree distance measures in MRI can be identical to micro-CT.

Overall, no other publicly available template or atlas of the inner ear has assembled and published a comprehensive list of inner ear landmarks for distance measurements. It should be noted that the literature-oriented landmark annotation in our work was time-consuming and non-trivial. By publicly providing these landmarks along with our templates and segmentations, we hope to provide a reproducible and consistent basis for such measurements in future studies as well as to pave the road for population-based standard values. Recently, another inner ear MRI template was presented, albeit including the application of Gadolinium contrast agent and with a less extensive quantitative assessment of template morphology, without investigation of potential confounds, and with separate (i.e. biased) templates for the left and right ear [71]. In comparison, we created an unbiased template and atlas, with detailed labels for sub-structures of the semicircular duct system, vestibule and cochlea. These were obtained through manual labelling and registration of an atlas from micro-CT [20]. We validated the template and atlas by performing a morphometric analysis of the semicircular canals, vestibule and cochlea, and by comparing anatomical measurements to established measures from literature.

It is important to note that the multi-sequence intensity templates provide a lot of flexibility for usage of this atlas. Future studies based on T1-, T2-weighted data and CISS-sequences can directly utilize the provided templates through intra-modal atlas registration (in a single- or multi-variate approach). Other structural MRI sequences (with or without contrast), MRI paradigms (e.g. diffusion-weighted MRI) or even other modalities (e.g. CT, micro-CT)

can still register and utilize the atlas through multi-modal image similarity functions (e.g. normalized mutual information).

Our atlas deviates slightly from the related literature, in particular regarding volumetric measures. For example, the overall inner ear volume appears to be marginally over-estimated. This may be due to partial volume effects and signal blurring after template building. Other volumetric measures like the ampullae look to be slightly under-estimated compared to the literature. This is likely due to simplified geometric assumptions for anatomic shapes made by the authors in the previous work [67], e.g. a sphere for the ampullae. These simplifications were probably helpful in this pioneering study, which approximated 3D volumes through 2D cross-cuts but should be dropped in the long run at higher resolutions to reach anatomical ground truth. Materials like our 3D templates and surface meshes should allow for more accurate volumetric and thus more realistic measurements. Overall, it is remarkable in our opinion that the outer surface of the inner ear in the T2-weighted template (i.e. the Otsu-threshold iso-surface) seems to very accurately represent the outer surface of bony structures as measured by micro-CT, a result that was not expected prior to the conductance of this study. This result in return then also justifies the surface-based co-registration of the bony surface mesh from Ariadne to our T2 iso-surface, in order to transfer internal surface meshes into our template.

Implications. Our atlas can be applied for localization, segmentation and sub-parcellations of the entire human inner ear for clinical and scientific questions. With co-registration to the template, individual differences can be detected (e.g. of the anatomical structures itself or with respect to deviations from Reid's plane). The atlas may also be helpful for surgical planning of implanting the electrodes of cochlear or vestibular implants. Even though malformations were not used to build our atlas, image-based registration is often robust enough to compensate for a wide range of deformations, such that we expect the material to be useful for in-vivo detection and comparison of morphological abnormalities of the inner ear structures as well.

Limitations. Despite the high isotropic voxel resolution of 0.2 mm in our final template, our results still do not resolve every fine detail of the inner ear, especially not of the auditory aspects. We were able to visualize the three major parts of the cochlea (the scala vestibuli, the scala tympani and the cochlear duct), but the results were still insufficient for e.g. a visualization of the organ of corti that lies inside the cochlear duct and houses the hair cells. The same holds true for the structure inside the ampullae: the cupulae. These structures are not ossified and it is far more complex to detect them with 3T MRI contrasts due to the tissue type, achievable isotropic resolution, and mitigating head motion during data acquisition. In this context, it seems feasible and realistic to achieve improvements to the resolution of a high-resolution T2-SPACE with coverage of the temporal bone alone and the CISS sequence in the target range of 0.4mm. It should further be noted as a limitation that the cohort's mean age was 26 +/- 2.3 years, i.e. after development of a fully formed adult human skull. Changes due to age cannot be addressed within our cohort. However, we would not expect a change in bony structures in elderly patients with hearing or vestibular problems. Typically, a degeneration of soft tissue like hair cells in the organ of corti or the cochlear nerve lead to age related hearing loss. Further inner ear malformations reported previously [70] are not represented by our atlas, since we only investigated MRI images of normal subjects. Nonetheless, as noted, malformations may well be detectable as significant structural deviations, through co-registration and overlay on our template on a subject-basis.

Future Work. There are several ways in which the proposed inner ear atlas can be extended. First, the atlas can be augmented with additionally labelled regions nearby. The auditory and the two vestibular nerves appear as separable structures in the templates and are hence of particular interest, but were out of scope for this inaugural study. Once these nerves are included, the facial nerve can as well be segmented as it runs in close proximity of the vestibule. Similar to the inner ear micro-CT atlas [20] used in this work, other micro-CT atlases as in [29] can help in identifying and accurately delineating nerves, vas-

culature and bones in our template space. For nerves, the T1-weighted template could become more relevant than in this study. In T1, nerve structures are not only visible (compared to the rest of the inner ear structures), but they have a complementary, hyper-intense appearance, while appearing hypo-intense in the T2 and CISS templates (see Figure 4, panel C). Adding the angles of the semicircular canals towards each other on a single-subject basis and analysing the coplanarity of functional pairs [72], together with the orientation of the eye muscles can further increase the clinical relevance of our IE-Map atlas. Another next step is to develop an automatic segmentation method for prospective validation and application of the templates and atlas. In initial registration experiments, we have verified that segmentation of new subjects is possible using pair-wise single- and multi-variate image registration methods, again provided by ANTs [19]. A fully automatic segmentation method would require the tool-chaining of left and right inner ear localization, template displacement, and local deformation to the inner ear structures of test subjects. The implementation and validation of such a toolkit is also left for future work. A further exciting avenue for improvement stems from the multi-modal fusion of our in-vivo template with micro-CT volumes from multiple subjects. In-vivo MRI may never resolve a similarly fine-grained structural information as micro-CT, but we have demonstrated the feasibility of geometric fusion through multi-variate image registration and surface alignment. Eventually, this could allow for the construction of probabilistic label maps in micro-meter resolution, within the unbiased geometry of our template space.

5. Conclusion

In this work, we presented a comprehensive human inner ear atlas and three unbiased templates. Data were acquired in-vivo in a completely non-invasive approach from the largest dedicated cohort for vestibular substructures to date. Semimanual segmentation allowed for successful quantitative assessment of all relevant vestibular and auditory substructures of the inner ear and landmark-

based annotation. Total intracranial volume was found to be a confounding covariate with inner ear measurements. We found no differences in inner ear measurements with respect to gender or ear. Due to the absence of laterality effects, a single unified multi-variate template and atlas was published. It is our hope and aim that template and atlas can find application in numerous domains and disciplines studying neurootological health and disease. Potential applications include inner ear localization, segmentation and sub-parcellation, to quantitatively assess peripheral vestibular and auditory anatomy in group comparisons as well as over the course of longitudinal studies. By providing the templates, atlas segmentation, surface meshes and landmark annotations freely and publicly, we hope to provide clinicians and researchers in neurology, neuroscience and otorhinolaryngology with a new tool and robust basis as a starting point for computational neuro-otology grounded in neuroimaging.

Data availability

The atlas material in this repository can be downloaded and used for non-commercial purposes from our public github repository under the URL:
<https://github.com/pydsgz/IEMap>.

Acknowledgements

The study was supported by the German Federal Ministry of Education and Research (BMBF) in connection with the foundation of the German Center for Vertigo and Balance Disorders (DSGZ) (grant number 01 EO 0901), and a stipend of the Graduate School of Systemic Neurosciences (DFG-GSC 82/3) to Theresa Raiser. We thank Paul Taylor for critical input and feedback.

References

- [1] A. C. Evans, A. L. Janke, D. L. Collins, S. Baillet, Brain templates and atlases, *Neuroimage* 62 (2) (2012) 911–922. [doi:10.1016/j.neuroimage.2012.01.024](https://doi.org/10.1016/j.neuroimage.2012.01.024).

- [2] S. Ewert, P. Plettig, N. Li, M. M. Chakravarty, D. L. Collins, T. M. Herrington, A. A. Kühn, A. Horn, Toward defining deep brain stimulation targets in mni space: a subcortical atlas based on multimodal mri, histology and structural connectivity, *Neuroimage* 170 (2018) 271–282.
[doi:10.1016/j.neuroimage.2017.05.015](https://doi.org/10.1016/j.neuroimage.2017.05.015).
- [3] T. E. Behrens, H. Johansen-Berg, M. Woolrich, S. Smith, C. Wheeler-Kingshott, P. Boulby, G. Barker, E. Sillery, K. Sheehan, O. Ciccarelli, et al., Non-invasive mapping of connections between human thalamus and cortex using diffusion imaging, *Nature neuroscience* 6 (7) (2003) 750. [doi:10.1038/nn1075](https://doi.org/10.1038/nn1075).
- [4] J. Diedrichsen, J. H. Balsters, J. Flavell, E. Cussans, N. Ramnani, A probabilistic mr atlas of the human cerebellum, *Neuroimage* 46 (1) (2009) 39–46.
[doi:10.1016/j.neuroimage.2009.01.045](https://doi.org/10.1016/j.neuroimage.2009.01.045).
- [5] B. De Leener, V. S. Fonov, D. L. Collins, V. Callot, N. Stikov, J. Cohen-Adad, Pam50: unbiased multimodal template of the brainstem and spinal cord aligned with the icbm152 space, *Neuroimage* 165 (2018) 170–179. [doi:10.1016/j.neuroimage.2017.10.041](https://doi.org/10.1016/j.neuroimage.2017.10.041).
- [6] M. Milchenko, S. A. Norris, K. Poston, M. C. Campbell, M. Ushe, J. S. Perlmutter, A. Z. Snyder, 7T MRI subthalamic nucleus atlas for use with 3T MRI, *Journal of Medical Imaging* 5 (01) (2018) 1. [doi:10.1117/1.jmi.5.1.015002](https://doi.org/10.1117/1.jmi.5.1.015002).
- [7] M. C. Keuken, P.-L. Bazin, L. Crown, J. Hootsmans, A. Laufer, C. Müller-Axt, R. Sier, E. J. van der Putten, A. Schäfer, R. Turner, B. U. Forstmann, Quantifying inter-individual anatomical variability in the subcortex using 7T structural MRI, *NeuroImage* 94 (2014) 40–46. [doi:10.1016/j.neuroimage.2014.03.032](https://doi.org/10.1016/j.neuroimage.2014.03.032).
- [8] J. H. Noble, R. F. Labadie, O. Majdani, B. M. Dawant, Automatic segmentation of intracochlear anatomy in conventional ct, *IEEE Transactions*

on Biomedical Engineering 58 (9) (2011) 2625–2632. [doi:10.1109/TBME.2011.2160262](https://doi.org/10.1109/TBME.2011.2160262).

- [9] F. A. Reda, T. R. McKracken, R. F. Labadie, B. M. Dawant, J. H. Noble, Automatic segmentation of intra-cochlear anatomy in post-implantation ct of unilateral cochlear implant recipients, Medical Image Analysis 18 (3) (2014) 605–615. [doi:10.1016/j.media.2014.02.001](https://doi.org/10.1016/j.media.2014.02.001).
- [10] G. Grabner, A. L. Janke, M. M. Budge, D. Smith, J. Pruessner, D. L. Collins, Symmetric atlasing and model based segmentation: an application to the hippocampus in older adults, Med Image Comput Comput Assist Interv Int Conf Med Image Comput Comput Assist Interv 9 (2006) 58–66. [doi:10.1007/11866763_8](https://doi.org/10.1007/11866763_8).
- [11] J. M. Goldberg, V. J. Wilson, D. E. Angelaki, K. E. Cullen, J. Buttner-Ennever, K. Fukushima, The vestibular system: a sixth sense, Oxford University Press, 2012.
- [12] T. Demarcy, C. Vandersteen, N. Guevara, C. Raffaelli, D. Gnansia, N. Ayache, H. Delingette, Automated analysis of human cochlea shape variability from segmented micro-ct images, Computerized Medical Imaging and Graphics 59 (2017) 1–12. [doi:10.1016/j.compmedimag.2017.04.002](https://doi.org/10.1016/j.compmedimag.2017.04.002).
- [13] T. Brandt, Vertigo: Its Multisensory Syndromes, Springer London, 1991. [doi:10.1007/978-1-4471-3342-1](https://doi.org/10.1007/978-1-4471-3342-1).
- [14] L. Sennaroğlu, M. D. Bajin, Classification and current management of inner ear malformations, Balkan medical journal 34 (5) (2017) 397–411.
- [15] M. Strupp, T. Brandt, Peripheral vestibular disorders, Current opinion in Neurology 26 (1) (2013) 81–89.
- [16] P. Gunz, M. Ramsier, M. Kuhrig, J.-J. Hublin, F. Spoor, The mammalian bony labyrinth reconsidered, introducing a comprehensive geometric morphometric approach, Journal of Anatomy 220 (6) (2012) 529–543. [doi:10.1111/j.1469-7580.2012.01493.x](https://doi.org/10.1111/j.1469-7580.2012.01493.x).

- [17] A. Klein, J. Andersson, B. A. Ardekani, J. Ashburner, B. Avants, M. C. Chiang, G. E. Christensen, D. L. Collins, J. Gee, P. Hellier, J. H. Song, M. Jenkinson, C. Lepage, D. Rueckert, P. Thompson, T. Vercauteren, R. P. Woods, J. J. Mann, V. R. Parsey, Evaluation of 14 nonlinear deformation algorithms applied to human brain MRI registration, *NeuroImage* 46 (3) (2009) 786–802. [doi:10.1016/j.neuroimage.2008.12.037](https://doi.org/10.1016/j.neuroimage.2008.12.037).
- [18] T. Heimann, H.-p. Meinzer, Statistical shape models for 3d medical image segmentation : A review, *Medical Image Analysis* 13 (4) (2009) 543–563. [doi:10.1016/j.media.2009.05.004](https://doi.org/10.1016/j.media.2009.05.004).
- [19] B. B. Avants, P. Yushkevich, J. Pluta, D. Minkoff, M. Korczykowski, J. Detre, J. C. Gee, The optimal template effect in hippocampus studies of diseased populations, *NeuroImage* 49 (3) (2010) 2457–2466. [doi:10.1016/j.neuroimage.2009.09.062](https://doi.org/10.1016/j.neuroimage.2009.09.062).
- [20] R. David, A. Stoessel, A. Berthoz, F. Spoor, D. Bennequin, Assessing morphology and function of the semicircular duct system: Introducing new in-situ visualization and software toolbox, *Scientific Reports* 6 (32772). [doi:10.1038/srep32772](https://doi.org/10.1038/srep32772).
- [21] R. Glueckert, L. Johnson Chacko, D. Schmidbauer, T. Potrusil, E. J. Pechriggl, R. Hoermann, E. Brenner, A. Reka, A. Schrott-Fischer, S. Handschuh, Visualization of the Membranous Labyrinth and Nerve Fiber Pathways in Human and Animal Inner Ears Using MicroCT Imaging, *Frontiers in Neuroscience* 12 (2018) 501. [doi:10.3389/fnins.2018.00501](https://doi.org/10.3389/fnins.2018.00501).
- [22] A. V. Schweizer, R. Lebrun, L. A. Wilson, L. Costeur, T. Schmelzle, M. R. Sánchez-Villagra, Size variation under domestication: Conservatism in the inner ear shape of wolves, dogs and dingoes, *Scientific reports* 7 (1) (2017) 13330.
- [23] A. Postnov, A. Zarowski, D. N. Clerck, F. Vanpoucke, F. E. Offeciers, V. D. Dyck, S. Peeters, High resolution micro-{ct} scanning as an in-

novatory tool for evaluation of the surgical positioning of cochlear implant electrodes, *Acta Oto-Laryngologica* 126 (5) (2006) 467–474. [doi:10.1080/00016480500437377](https://doi.org/10.1080/00016480500437377).

- [24] H. M. Kjer, J. Fagertun, S. Vera, M. A. González Ballester, R. R. Paulsen, Shape modelling of the inner ear from micro-ct data, in: Proceedings of Symposium on Statistical Shape Models & Applications, Shape 2014, 2014, p. 21, poster presentation.
- [25] N. Gerber, M. Reyes, L. Barazzetti, H. M. Kjer, S. Vera, M. Stauber, P. Mistrik, M. Ceresa, N. Mangado, W. Wimmer, T. Stark, R. R. Paulsen, S. Weber, M. Caversaccio, M. A. G. Ballester, A multiscale imaging and modelling dataset of the human inner ear, *Scientific Data* 4 (2017) 170132. [doi:10.1038/sdata.2017.132](https://doi.org/10.1038/sdata.2017.132).
- [26] C. Schmidt, J. Harbort, R. Knecht, U. Grzyska, A. Muenscher, C. V. Dalchow, Measurement and comparison of labyrinthine structures with the digital volume tomography: ancient Egyptian mummies' versus today's temporal bones, *European Archives of Oto-Rhino-Laryngology* 270 (3) (2013) 831–840. [doi:10.1007/s00405-012-2047-y](https://doi.org/10.1007/s00405-012-2047-y).
URL <http://link.springer.com/10.1007/s00405-012-2047-y>
- [27] E. G. Ekdale, Form and function of the mammalian inner ear, *Journal of Anatomy* 228 (2) (2016) 324–337. [doi:10.1111/joa.12308](https://doi.org/10.1111/joa.12308).
URL <http://doi.wiley.com/10.1111/joa.12308>
- [28] T. van den Boogert, M. van Hoof, S. Handschuh, R. Glueckert, N. Guinand, J.-P. Guyot, H. Kingma, A. Perez-Fornos, B. Seppen, L. Johnson Chacko, A. Schrott-Fischer, R. van de Berg, Optimization of 3d-Visualization of Micro-Anatomical Structures of the Human Inner Ear in Osmium Tetroxide Contrast Enhanced Micro-CT Scans, *Frontiers in Neuroanatomy* 12 (2018) 41. [doi:10.3389/fnana.2018.00041](https://doi.org/10.3389/fnana.2018.00041).
URL <https://www.frontiersin.org/article/10.3389/fnana.2018.00041/full>

- [29] R. Gupta, S. H. Bartling, S. K. Basu, W. R. Ross, H. Becker, A. Pfoh, T. Brady, H. D. Curtin, Experimental flat-panel high-spatial-resolution volume ct of the temporal bone, *American journal of neuroradiology* 25 (8) (2004) 1417–1424.
- [30] J. S. Iyer, N. Zhu, S. Gasilov, H. M. Ladak, S. K. Agrawal, K. M. Stankovic, Visualizing the 3d cytoarchitecture of the human cochlea in an intact temporal bone using synchrotron radiation phase contrast imaging, *Biomedical Optics Express* 9 (8) (2018) 3757. [doi:10.1364/boe.9.003757](https://doi.org/10.1364/boe.9.003757).
- [31] D. S. Thylur, R. E. Jacobs, J. L. Go, A. W. Toga, J. K. Niparko, Ultra-high-field magnetic resonance imaging of the human inner ear at 11.7 tesla, *Otology & neurotology: official publication of the American Otological Society, American Neurotology Society [and] European Academy of Otology and Neurotology* 38 (1) (2017) 133.
- [32] H. Uzun, I. S. Curthoys, >. S. Jones, [A new approach to visualizing the membranous structures of the inner ear – high resolution X-ray micro-tomography](#), *Acta Oto-Laryngologica* 127 (6) (2007) 568–573. [doi:10.1080/00016480600951509](https://doi.org/10.1080/00016480600951509).
URL <http://www.tandfonline.com/doi/full/10.1080/00016480600951509>
- [33] J.-Y. Lee, K.-J. Shin, J.-N. Kim, J.-Y. Yoo, W.-C. Song, K.-S. Koh, A morphometric study of the semicircular canals using micro-ct images in three-dimensional reconstruction, *The Anatomical Record* 296 (5) (2013) 834–839.
- [34] W. Daocai, W. Qing, W. Ximing, H. Jingzhen, L. Cheng, M. Xiangxing, Size of the semicircular canals measured by multidetector computed tomography in different age groups, *Journal of Computer Assisted Tomography* 38 (2) (2014) 196–199. [doi:10.1097/rct.0b013e3182aaf21c](https://doi.org/10.1097/rct.0b013e3182aaf21c).
- [35] R. Lingam, S. Connor, J. Casselman, T. Beale, *Mri in otology: applications*

- in cholesteatoma and ménière's disease, Clinical Radiology 73 (1) (2018) 35–44. [doi:10.1016/j.crad.2017.09.002](https://doi.org/10.1016/j.crad.2017.09.002).
- [36] S. Naganawa, T. Nakashima, Visualization of endolymphatic hydrops with mr imaging in patients with ménière's disease and related pathologies: current status of its methods and clinical significance, Japanese Journal of Radiology 32 (4) (2014) 191–204. [doi:10.1007/s11604-014-0290-4](https://doi.org/10.1007/s11604-014-0290-4).
- [37] J. H. Keller, B. E. Hirsch, R. S. Marovich, B. F. Branstetter IV, Detection of endolymphatic hydrops using traditional mr imaging sequences, American journal of otolaryngology 38 (4) (2017) 442–446. [doi:10.1016/j.amjoto.2017.01.038](https://doi.org/10.1016/j.amjoto.2017.01.038).
- [38] M. Van der Jagt, W. Brink, M. Versluis, S. Steens, J. Briaire, A. Webb, J. Frijns, B. Verbist, Visualization of human inner ear anatomy with high-resolution mr imaging at 7t: initial clinical assessment, American Journal of Neuroradiology 36 (2) (2015) 378–383. [doi:10.3174/ajnr.A4084](https://doi.org/10.3174/ajnr.A4084).
- [39] E. L. van den Burg, M. van Hoof, A. Postma, A. M. L. Janssen, R. J. Stokroos, H. Kingma, R. van de Berg, An exploratory study to detect meniere's disease in conventional mri scans using radiomics, Frontiers in neurology 7 (2016) 190. [doi:10.3389/fneur.2016.00190](https://doi.org/10.3389/fneur.2016.00190).
- [40] F. G. Gonçalves, L. L. F. do Amaral, Constructive interference in steady state imaging in the central nervous system, European Neurological Review 6 (2011) 138–42. [doi:10.17925/ENR.2011.06.02.138](https://doi.org/10.17925/ENR.2011.06.02.138).
- [41] H. Inui, T. Sakamoto, T. Ito, T. Kitahara, Volumetric measurements of the inner ear in patients with meniere's disease using three-dimensional magnetic resonance imaging, Acta oto-laryngologica 136 (9) (2016) 888–893. [doi:10.3109/00016489.2016.1168940](https://doi.org/10.3109/00016489.2016.1168940).
- [42] J. Cho, H. Cheon, J. H. Park, H.-J. Lee, H.-J. Kim, H. G. Choi, J.-W. Koo, S. K. Hong, Sudden sensorineural hearing loss associated with inner ear lesions detected by magnetic resonance imaging, PLOS ONE 12 (10)

- (2017) e0186038. [doi:10.1371/journal.pone.0186038](https://doi.org/10.1371/journal.pone.0186038)
URL <http://dx.plos.org/10.1371/journal.pone.0186038>
- [43] D. Hingwala, S. Chatterjee, C. Kesavadas, B. Thomas, T. R. Kapilamoorthy, Applications of 3d ciss sequence for problem solving in neuroimaging, *The Indian journal of radiology & imaging* 21 (2) (2011) 90. [doi:10.4103/0971-3026.82283](https://doi.org/10.4103/0971-3026.82283).
- [44] O. Esteban, D. Birman, M. Schaer, O. O. Koyejo, R. A. Poldrack, K. J. Gorgolewski, Mriqc: Advancing the automatic prediction of image quality in mri from unseen sites, *PloS one* 12 (9) (2017) e0184661. [doi:10.1371/journal.pone.0184661](https://doi.org/10.1371/journal.pone.0184661).
- [45] N. J. Tustison, B. B. Avants, P. A. Cook, Y. Zheng, A. Egan, P. A. Yushkevich, J. C. Gee, N4itk: Improved n3 bias correction, *IEEE Transactions on Medical Imaging* 29 (6) (2010) 1310–1320. [doi:10.1109/TMI.2010.2046908](https://doi.org/10.1109/TMI.2010.2046908).
- [46] B. H. Menze, A. Jakab, S. Bauer, J. Kalpathy-Cramer, K. Farahani, J. Kirby, Y. Burren, N. Porz, J. Slotboom, R. Wiest, L. Lanczi, E. Gerstner, M. A. Weber, T. Arbel, B. B. Avants, N. Ayache, P. Buendia, D. L. Collins, N. Cordier, J. J. Corso, A. Criminisi, T. Das, H. Delingette, C. Demiralp, C. R. Durst, M. Dojat, S. Doyle, J. Festa, F. Forbes, E. Geremia, B. Glocker, P. Golland, X. Guo, A. Hamamci, K. M. Iftekharuddin, R. Jena, N. M. John, E. Konukoglu, D. Lashkari, J. A. Mariz, R. Meier, S. Pereira, D. Precup, S. J. Price, T. R. Raviv, S. M. Reza, M. Ryan, D. Sarikaya, L. Schwartz, H. C. Shin, J. Shotton, C. A. Silva, N. Sousa, N. K. Subbanna, G. Szekely, T. J. Taylor, O. M. Thomas, N. J. Tustison, G. Unal, F. Vasseur, M. Wintermark, D. H. Ye, L. Zhao, B. Zhao, D. Zikic, M. Prastawa, M. Reyes, K. Van Leemput, The multimodal brain tumor image segmentation benchmark (brats), *IEEE Transactions on Medical Imaging* 34 (10) (2015) 1993–2024. [doi:10.1109/TMI.2014.2377694](https://doi.org/10.1109/TMI.2014.2377694).
- [47] N. Finby, K.-Y. Chynn, Cranial computerized tomography: Technique and

- anatomy, in: Manual of Cranial Computerized Tomography, S. Karger {AG}, 1982, pp. 15–29. [doi:10.1159/000406259](https://doi.org/10.1159/000406259).
- [48] C. C. Della Santina, V. Potyagaylo, A. A. Migliaccio, L. B. Minor, J. P. Carey, Orientation of human semicircular canals measured by three-dimensional multiplanar ct reconstruction, Journal of the Association for Research in Otolaryngology 6 (3) (2005) 191–206. [doi:10.1007/s10162-005-0003-x](https://doi.org/10.1007/s10162-005-0003-x).
- [49] R. Blanks, I. Curthoys, C. Markham, Planar relationships of the semi-circular canals in man, Acta oto-laryngologica 80 (1-6) (1975) 185–196. [doi:10.3109/00016487509121318](https://doi.org/10.3109/00016487509121318).
- [50] S. Hashimoto, H. Naganuma, K. Tokumasu, A. Itoh, M. Okamoto, Three-dimensional reconstruction of the human semicircular canals and measurement of each membranous canal plane defined by reid's stereotactic coordinates, Annals of Otology, Rhinology & Laryngology 114 (12) (2005) 934–938. [doi:10.1177/000348940511401207](https://doi.org/10.1177/000348940511401207).
- [51] N. Otsu, A threshold selection method from gray level histograms, IEEE Transactions on Systems, Man, and Cybernetics 9 (1) (1979) 62–66. [doi:10.1109/TSMC.1979.4310076](https://doi.org/10.1109/TSMC.1979.4310076).
- [52] P.-E. Danielsson, Euclidean distance mapping, Computer Graphics and Image Processing 14 (3) (1980) 227–248. [doi:10.1016/0146-664X\(80\)90054-4](https://doi.org/10.1016/0146-664X(80)90054-4).
- [53] A. Fedorov, R. Beichel, J. Kalpathy-Cramer, J. Finet, J. C. Fillion-Robin, S. Pujol, C. Bauer, D. Jennings, F. Fennessy, M. Sonka, J. Buatti, S. Aylward, V. J. Miller, S. Pieper, R. Kikinis, 3d slicer as an image computing platform for the quantitative imaging network, Magnetic Resonance Imaging 30 (9) (2012) 1323–1341. [doi:10.1016/j.mri.2012.05.001](https://doi.org/10.1016/j.mri.2012.05.001).
- [54] B. C. Lowekamp, D. T. Chen, L. Ibáñez, D. Blezek, The design of sim-

pleitk, Frontiers in neuroinformatics 7 (2013) 45. [doi:10.3389/fninf.2013.00045](https://doi.org/10.3389/fninf.2013.00045).

- [55] E. M. Sugihara, A. L. Marinica, N. D. Vandjelovic, B. M. Kelley, S. S. Sana, N. E. Starkey, S. C. Babu, Mastoid and Inner Ear Measurements in Patients With Meniere's Disease, *Otology & Neurotology* 38 (10) (2017) 1484–1489. [doi:10.1097/MAO.0000000000001576](https://doi.org/10.1097/MAO.0000000000001576).
- [56] M. T. Teixido, G. Kirkilas, P. Seymour, K. Sem, A. Iaia, O. Sabra, H. Isildak, Normative Inner Ear Volumetric Measurements:, *The Journal of Craniofacial Surgery* 26 (1) (2015) 251–254. [doi:10.1097/SCS.0000000000001204](https://doi.org/10.1097/SCS.0000000000001204).
- [57] Y.-K. Liu, C.-L. Qi, J. Tang, M.-L. Jiang, L. Du, Z.-H. Li, S.-H. Tan, A.-Z. Tang, The diagnostic value of measurement of cochlear length and height in temporal bone CT multiplanar reconstruction of inner ear malformation, *Acta Oto-Laryngologica* 137 (2) (2017) 119–126. [doi:10.1080/00016489.2016.1221132](https://doi.org/10.1080/00016489.2016.1221132).
- [58] D. Purcell, J. Johnson, N. Fischbein, A. K. Lalwani, Establishment of normative cochlear and vestibular measurements to aid in the diagnosis of inner ear malformations, *Otolaryngology—Head and Neck Surgery* 128 (1) (2003) 78–87. [doi:10.1067/mhn.2003.51](https://doi.org/10.1067/mhn.2003.51).
- [59] H. Shim, J.-E. Shin, J. Chung, K.-S. Lee, Inner ear anomalies in cochlear implantees: Importance of radiologic measurements in the classification, *Otology and Neurotology* 27 (6) (2006) 831–837. [doi:10.1097/01.mao.0000227902.47483.ef](https://doi.org/10.1097/01.mao.0000227902.47483.ef).
- [60] H. W. Lilliefors, [On the Kolmogorov-Smirnov Test for Normality with Mean and Variance Unknown](#), *Journal of the American Statistical Association* 62 (318) (1967) 399–402. [doi:10.1080/01621459.1967.10482916](https://doi.org/10.1080/01621459.1967.10482916).
URL <http://www.tandfonline.com/doi/abs/10.1080/01621459.1967.10482916>

- [61] Y. Benjamini, Y. Hochberg, Controlling the false discovery rate: a practical and powerful approach to multiple testing, *Journal of the Royal statistical society: series B (Methodological)* 57 (1) (1995) 289–300. [doi:
http://dx.doi.org/10.2307/2346101](http://dx.doi.org/10.2307/2346101).
- [62] L. M. O'Brien, D. A. Ziegler, C. K. Deutsch, J. A. Frazier, M. R. Herbert, J. J. Locascio, Statistical adjustments for brain size in volumetric neuroimaging studies: Some practical implications in methods, *Psychiatry Research: Neuroimaging* 193 (2) (2011) 113–122. [doi:
10.1016/j.pscychresns.2011.01.007](https://doi.org/10.1016/j.pscychresns.2011.01.007).
URL [https://linkinghub.elsevier.com/retrieve/pii/
S0925492711000357](https://linkinghub.elsevier.com/retrieve/pii/S0925492711000357)
- [63] E. Jones, T. Oliphant, P. Peterson, et al., Scipy: Open source scientific tools for python[Online; accessed 06. Dec. 2017].
- [64] R. Vallat, Pingouin: Statistics in python, *The Journal of Open Source Software* 3 (31) (2018) 1026.
- [65] S. Seabold, J. Perktold, Statsmodels: Econometric and statistical modeling with python, in: 9th Python in Science Conference, 2010.
- [66] M. Mahesh, The Essential Physics of Medical Imaging, Third Edition., *Medical Physics* 40 (7) (2013) 077301. [doi:
10.1118/1.4811156](https://doi.org/10.1118/1.4811156).
URL <http://doi.wiley.com/10.1118/1.4811156>
- [67] R. A. Buckingham, G. E. Valvassori, Inner Ear Fluid Volumes and the Resolving Power of Magnetic Resonance Imaging: Can it Differentiate Endolymphatic Structures?, *Annals of Otology, Rhinology & Laryngology* 110 (2) (2001) 113–117. [doi:
10.1177/000348940111000204](https://doi.org/10.1177/000348940111000204).
- [68] B. Escudé, C. James, O. Deguine, N. Cochard, E. Eter, B. Fraysse, The Size of the Cochlea and Predictions of Insertion Depth Angles for Cochlear Implant Electrodes, *Audiology and Neurotology* 11 (1) (2006) 27–33. [doi:
10.1159/000095611](https://doi.org/10.1159/000095611).

- [69] M. Igarashi, T. O-Uchi, H. Isago, W. K. Wright, Utricular and Saccular Volumetry in Human Temporal Bones, *Acta Oto-Laryngologica* 95 (1-4) (1983) 75–80. [doi:10.3109/00016488309130918](https://doi.org/10.3109/00016488309130918).
- [70] A. Dhanasingh, A. Dietz, C. Jolly, P. Roland, Human inner-ear malformation types captured in 3d, *The journal of international advanced otology* 15 (1) (2019) 77.
- [71] V. Kirsch, F. Nejatbakhshesfahani, S.-A. Ahmadi, M. Dieterich, B. Ertl-Wagner, **A probabilistic atlas of the human inner ear's bony labyrinth enables reliable atlas-based segmentation of the total fluid space**, *Journal of Neurology* 266 (S1) (2019) 52–61. [doi:10.1007/s00415-019-09488-6](https://doi.org/10.1007/s00415-019-09488-6)
URL <http://link.springer.com/10.1007/s00415-019-09488-6>
- [72] D.-K. Kim, D.-R. Kim, S. H. Jeong, G. J. Kim, K.-H. Chang, B.-C. Jun, **Analysis of the coplanarity of functional pairs of semicircular canals using three-dimensional images reconstructed from temporal bone magnetic resonance imaging**, *The Journal of Laryngology & Otology* 129 (5) (2015) 430–434. [doi:10.1017/S0022215115000201](https://doi.org/10.1017/S0022215115000201).
URL https://www.cambridge.org/core/product/identifier/S0022215115000201/type/journal_article